Fourier finite-difference wave-equation migration in tilted transversely isotropic media with an improved solution for coefficient estimation

Chen Tang, Yang He, Jian Mao, Jianming Sheng, TGS*

Summary

We develop an improved scheme for the coefficient estimation in the Fourier finite-difference (FFD) wave-equation migration (WEM) in 3D tilted transversely isotropic (TTI) media. The FFD requires using a group of coefficients to approximate the square root operator that is generated from the wavefield decomposition. An accurate estimation of these coefficients in the four-way splitting requires solving a nonlinear least-squares problem. The solution is easy to fall into a local minimum and thus requires good initial inputs. The proposed solution involves three steps: The first step is to estimate the coefficients in the *x* and *y* directions. This process can be linearized by selecting the phase angles at 0° and 90°. By using the coefficients in the *x*- and *y*-directions that are obtained from step one, the second step is to estimate the coefficients in the *m*- and *p*-directions by selecting the phase angles at 45° and -45°. This is certainly a rough approximation because the two groups of coefficients (one is for the *x*- and *y*-directions and the other is for the *m*- and *p*-directions) cannot be cascaded, but they can be used as the initial values for the nonlinear inversion. So, in the third step, we apply the nonlinear inversion to improve the accuracy of the coefficients. After calculating these coefficients, we describe the scheme to implement the four-way splitting FFD propagator in the TTI media and then use this propagator to produce the WEM image. The numerical and real-data examples have shown the validity of our methodology and flow.

Introduction

Although reverse time migration (RTM) has shown its advantages in complex subsurface imaging, the one-way wave-equation migration (WEM) retains its value for the areas without the demand of imaging some complex structures such as the subsalt. Different from the full wavefield extrapolation that is used for RTM and theoretically may require an expensive wavefield decomposition to remove backscattering artifacts, the Fourier finite-difference (FFD) directly extrapolates the downgoing source and upgoing receiver wavefields. The FFD works in the frequency domain and so it requires less computational time per processor and is also suitable for providing the high-frequency imaging and using the deconvolution imaging condition. As the ray-based migration needs to smooth the high-resolution velocity produced by the FWI while the RTM is too expensive for producing high-frequency images, the WEM is a good method to fill this gap.

The WEM algorithms that have been used for transversely isotropic (TI) media include (but are not limited to) the generalized Phase screen (Xie and Wu, 2002), the implicit finite-difference (IFD) (e.g., Ristow and Ruhl, 1997) and the Fourier FD (FFD) (Ristow and Ruhl, 1994) methods. The generalized screen propagator (GSP) is more accurate than the traditional first order Taylor or Padé expansion at wide angles but is still not accurate enough for relatively-high propagation angles; besides, derivation of the GSP in the tilted TI (TTI) media is difficult.

To improve the accuracy, Shan (2006) uses least-squares fitting to estimate the coefficients for the IFD in the vertical TI (VTI) media. The method first uses the theoretical formulas to calculate the slowness-vector samples and then uses these samples to perform a least-squares estimation and give the coefficients of a designed formula. The method has the potential to give high-accuracy approximation for high angles and large lateral variations; the accuracy mainly depends on the order of the approximation formula. Because the VTI media is vertically symmetric, the approximation formula contains only even orders. Shan (2007) extends it into the TTI media by adding odd orders. His method includes two directions (*x* and *y*) in 3D. Valenciano et al. (2009) and Hua et al. (2010) extend this method into the four-way splitting (*x*, *y*, *m* and *p*) for the FFD and IFD, respectively. Hua et al. (2013) further develop the table-driven four-way splitting into high-order and propose an approximation method to decrease the size of the tables.

We use the FFD to give the WEM propagator in the TTI media (TTI FFD WEM). Calculation of the coefficients for the four-way splitting in 3D is a nonlinear problem. It is easy to fall into a local minimum; this may lead to an inaccurate or unstable propagation. To solve these problems, we develop a flow to improve the coefficient estimation. We also introduce several implementation strategies for the four-way splitting TTI FFD WEM.

Theory

Based on the work of Hua et al. (2010, 2013), the equation to estimate the coefficients for the four-way splitting TTI FFD propagator can be written as

$$\left(\bar{S}_z - S_{z0} - F\right) = -\sum_{n=x,y,m,p} \frac{c_n S_n + a_n S_n^2 + e_n S_n^3}{1 - b_n S_n^2 - d_n S_n}, \qquad (1)$$

where

$$F = \sqrt{\rho^2 - \left(S_x^2 + S_y^2\right)} - \rho = \sqrt{\left(v_p / v_{p0}\right)^2 - \left(S_x^2 + S_y^2\right)} - \left(v_p / v_{p0}\right). \qquad (2)$$

10.1190/segam2019-3214439.1

Here, $\bar{S}_z$ is the estimated *z*-component of the slowness vector. S_x and S_y are the *x*- and *y*-components. S_m and S_p are the (*y*+*x*) and (*y*-*x*) components. The a, b, c, d and e are coefficients. We have $\rho = v_p / v_{p0}$ where the v_{p0} is the reference vertical velocity for a depth. S_z is the *z*-component of the slowness vector and S_{z0} is the S_z at the polar angle $\theta_a = 0°$ and the azimuth angle $\phi_a = 0°$ of the phase direction of the propagating wavefield. Equation 1 is to estimate the $\bar{S}_z$ for a given (S_x, S_y). There is also a theoretical (S_x, S_y, S_z) that can be calculated from Tsvankin's (2005) formula. By minimizing the difference between $\bar{S}_z$ and S_z at all the (S_x, S_y) samples, four groups of coefficients (a,b,c,d,e) are calculated.

The least-squares estimation of these coefficients is a nonlinear inversion problem. The solution may fall into a local minimum and so initial values are important for the nonlinear inversion system. An approach is proposed to address this; we use a linear method to generate the initial values for the nonlinear inversion. The key for this linear method is to select the phase angle to isolate the parameter estimation in each of the *x*, *y*, *m* and *p* directions that correspond to phase angles 0°, 90°, 45°, –45°, respectively. This involves two parts. The first one is to provide a linear solution for the two-way splitting equation,

$$\left(\bar{S}_z - S_{z0} - F\right) = -\sum_{n=x,y} \frac{c_n S_n + a_n S_n^2 + e_n S_n^3}{1 - b_n S_n^2 - d_n S_n}, \tag{3}$$

When $\phi_a = 0°$, $S_y = 0$ and so equation 3 is totally dependent on S_x; when $\phi_a = 90°$, $S_x = 0$ and so equation 3 is totally dependent on S_y. Therefore,

$$\left(\bar{S}_z - S_{z0} - F\right) = \begin{cases} -\dfrac{c_x S_x + a_x S_x^2 + e_x S_x^3}{1 - b_x S_x^2 - d_x S_x}, \text{ when } \phi_a = 0°, \\ -\dfrac{c_y S_y + a_y S_y^2 + e_y S_y^3}{1 - b_y S_y^2 - d_y S_y}, \text{ when } \phi_a = 90°. \end{cases} \tag{4}$$

The coefficients calculated by the linear equation 4 can be used for the two-way (*x* and *y*) splitting and can also be used as the initial values for the four-way (*x*, *y*, *m* and *p*) splitting. To obtain the initial values for the *m*- and *p*-directions, we use

$$\left(\bar{S}_z - S_{z0} - F - G\right) = \begin{cases} -\dfrac{c_m S_m + a_m S_m^2 + e_m S_m^3}{1 - b_m S_m^2 - d_m S_m}, \text{ when } \phi_a = 45°, \\ -\dfrac{c_p S_p + a_p S_p^2 + e_p S_p^3}{1 - b_p S_p^2 - d_p S_p}, \text{ when } \phi_a = -45°, \end{cases} \tag{5}$$

where

$$G = -\frac{c_x S_x + a_x S_x^2 + e_x S_x^3}{1 - b_x S_x^2 - d_x S_x} - \frac{c_y S_y + a_y S_y^2 + e_y S_y^3}{1 - b_y S_y^2 - d_y S_y}. \tag{6}$$

Equation 5 certainly involves a rough approximation because it ignores the influence of the estimated *m*- and *p*-direction coefficients in equation 5 on the splitting equation 4 in the *x*- and *y*-directions. However, these coefficients can be used as the initial values for the nonlinear inversion. The final coefficients in the *x*-, *y*-, *m*- and *p*-directions are given by the nonlinear inversion. In this process, there are two options to approximate the gradients. The first one is to explicitly calculate the gradient in equation 1 and ignores the trade-offs between the *x*- and *y*-, and *m*- and *p*-directions; the second one is to use perturbations to implicitly estimate the gradient for equation 1. The first option is used to produce the examples in this paper. The inverse Hessian has also been estimated for the inversion. In summary, our approach for the coefficient estimation involves two steps. The first step uses a two-fold linear process (equations 3~6) to give the initial values for the nonlinear inversion. The second step uses a nonlinear inversion to give the coefficients.

Implementation

In the previous section, we describe the algorithm to estimate the coefficients in each splitting direction. To implement the FFD propagator, we need to convert equation 1 into a propagation equation in the frequency-space domain. If we define the forward and inverse Fourier transforms (FTs) as

$$\begin{cases} U(\omega, \mathbf{k}) = \int dt \int d\mathbf{x}\, u(t, \mathbf{x}) e^{i(\mathbf{kx} - \omega t)}, \\ u(t, \mathbf{x}) = \int d\omega \int d\mathbf{k}\, U(\omega, \mathbf{k}) e^{i(-\mathbf{kx} + \omega t)}, \end{cases} \tag{7}$$

we have

$$S_l = \left(v_p / \omega\right) k_l = -\left(v_p / i\omega\right) \partial / \partial l,\ l = x,\ y,\ z, \tag{8}$$

and so, equation 1 can be converted to three cascading parts

$$V = U e^{-i\sqrt{\left(\omega / v_{p0}\right)^2 - \left(k_x^2 + k_y^2\right)}\,\Delta z}, \tag{9}$$

$$W = V e^{-i\omega\left[\left(S_{z0} / v_p\right) - v_{p0}^{-1}\right]}, \tag{10}$$

and

$$\zeta \frac{\partial W}{\partial z} = -\sum_{n=x,y,m,p} \frac{c_n \zeta \dfrac{\partial W}{\partial n} + a_n \zeta^2 \dfrac{\partial^2 W}{\partial n^2} + e_n \zeta^3 \dfrac{\partial^3 W}{\partial n^3}}{1 - b_n \zeta^2 \dfrac{\partial^2}{\partial n^2} - d_n \zeta \dfrac{\partial}{\partial n}}, \tag{11}$$

where $\zeta = \left(-v_p / i\omega\right)$. Equation 9 is a phase-shift propagator (Gazdag, 1978). Equation 10 is a partial correction for lateral velocity variation. Equation 11 is a FD equation that is the core of the FFD propagator. The $-i$ in equations 9 and 10 depends on the definition of the forward and inverse FTs in equation 7 and will become i if we use an $i\omega$ in the forward FT and an $-i\omega$ in the inverse FT, which are used in our implementation. The implementation of equation 11 involves four cascading FD equations in the *x*-, *y*-, *m*- and *p*-directions and they are solved subsequently. The 3D

10.1190/segam2019-3214439.1

kernel in each direction consists of a group of 2D kernels. Take the *x*-direction for example, the implementation is to perform a 2D kernel along the *x*-direction at each sampling point in the *y* direction. This implementation is straightforward for the splitting in the *x*- and *y*-directions but becomes more complicated in the *m*- and *p*-directions because we need to input the data along the *m*- or *p*-direction into the corresponding 2D kernel. The 2D equation that can be obtained from setting $n = x$ in equation 11, is further converted into a linear equation system for implementation,

$$\Gamma \mathrm{X} = \Upsilon, \tag{12}$$

where Γ is a symmetric matrix (e.g., a triangle matrix for the simplest case), X is the array of the updated wavefield and Υ is the array calculated by a function of the current wavefield or the current and previous wavefields.

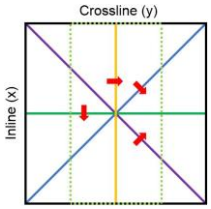

Figure 1: Sketch map for implementation of the four-way splitting in equation 11 at one depth. The red arrows on the green, orange, blue and purple lines mean that these lines are moving in *x*-, *y*-, *m*- and *p*-directions, respectively. The light green box indicates the case when $ny < nx$.

Figure 1 shows a sketch map to implement the four-way splitting. Each line means a 2D implementation in the 2D equation. The arrow can also point to the opposite direction; the implementation order in one arrow direction does not matter. Each line in one arrow direction is independent from others in the same direction; therefore, there is a potencial to implement all the lines in one arrow direction parallelly. For the *m*- and *p*-directions, there should be functions to collect the data in the *m*- or *p*-directions and input (output) it into (from) the 2D kernel. Take the *p*-direction for example, for a situation that $ny \le nx$, we have

$$\begin{cases} ix = \begin{cases} ip', & im \le nx, \\ nx - 1 - ip', & im > nx, \end{cases} \\ iy = \begin{cases} nx - np'(im) + ip' - (nx - ny)/2, & im \le nx, \\ np'(im) - 1 - ip' - (nx - ny)/2, & im > nx, \end{cases} \end{cases} \tag{13}$$

where the *ix*, *iy* and *im* are the indices for the *x*-, *y*- and *m*-directions, respectively and they start at zero. We define the *nx*, *ny* and *nm* as the total grid points in the *x*-, *y*- and *m*-directions. Here $nm = 2 \times nx + 1$. The *np'* is the total points in the *p*-direction when $nx = ny$ and varies with the *im*; the *ip'* is the index. For the case where $ny < nx$ (see the light green box in Figure 1), for some *ip'*, the corresponding *iy* are outside its range and then the wavefield at these *ip'* are set to zero. A potential choice is to use the *np* that is both *ny*- and *im*-dependent, to save the computational cost, which means the *ip* starts at zero when $iy = 0$ and ends at $np - 1$ when $iy = ny - 1$. The function for the *m*-direction can be obtained from that for the *p*-direction by using their symmetry.

Optimization

Calculation of the coefficients requires solving linear equations and implementing nonlinear inversions and thus it is expensive. To save the cost, we use the table-driven strategy (e.g., Shan, 2007; Hua et al., 2010). The tables are precalculated and can be reused for different tests or different models within a certain parameter range. As indicated by Hua et al. (2013), the coefficient tables for the TTI media have symmetries. Therefore, based on the coefficients for $\theta \subseteq [0°, 90°]$ and $\phi \subseteq [0°, 90°]$ (here, the θ and ϕ are the polar and azimuth angles of the TTI model, respectively), we can calculate the coefficients for the polar and azimuth angles that are not in this range. See Table 1. For a higher order approximation, the symmetries for odd orders should follow those of *a* and *b* and the symmetries for the even orders should follow those of *c*, *d* and *e*. To increase the computational speed, we do not use the third order (***e***) coefficients to produce the examples in this paper, but we do recommend using it to increase accuracy in strong anisotropic media. The sampling cannot be too small because of the limited memory. After the sampling intervals of the tables have been decided, to increase the accuracy, a 5D interpolation (the 5D corresponds to the five parameters in acoustic TTI media) is used and we choose a simple linear interpolation scheme. There is also another option that uses the V_p and coefficient models to replace the anisotropic model. These coefficients models can be calculated by either directly applying our solver or using the tables. Then the TTI FFD WEM do not need to input the anisotropic models and coefficient tables, instead we input the V_p and coefficient models.

	ax	bx	cx	dx	ex	ay	by	cy	dy	ey
0	ax_0	bx_0	cx_0	dx_0	ex_0	ay_0	by_0	cy_0	dy_0	ey_0
1	ax_0	bx_0	$-cx_0$	$-dx_0$	$-ex_0$	ay_0	by_0	$-cy_0$	$-dy_0$	$-ey_0$
2	ax_0	bx_0	cx_0	dx_0	ex_0	ay_0	by_0	$-cy_0$	$-dy_0$	$-ey_0$
3	ax_0	bx_0	$-cx_0$	$-dx_0$	$-ex_0$	ay_0	by_0	cy_0	dy_0	ey_0
	am	**bm**	**cm**	**dm**	**em**	**ap**	**bp**	**cp**	**dp**	**ep**
0	am_0	bm_0	cm_0	dm_0	em_0	ap_0	bp_0	cp_0	dp_0	ep_0
1	am_0	bm_0	$-cm_0$	$-dm_0$	$-em_0$	ap_0	bp_0	$-cp_0$	$-dp_0$	$-ep_0$
2	ap_0	bp_0	cp_0	dp_0	ep_0	am_0	bm_0	cm_0	dm_0	em_0
3	ap_0	bp_0	$-cp_0$	$-dp_0$	$-ep_0$	am_0	bm_0	$-cm_0$	$-dm_0$	$-em_0$

Table 1: The symmetries of the coefficients for the four-way splitting TTI FFD. Scripts 0, 1, 2, 3 respectively denote the angle ranges $(0° \le \theta \le 90°,\ 0° \le \phi \le 90°)$, $(-90° \le \theta \le 0°,\ 0° \le \phi \le 90°)$, $(0° \le \theta \le 90°,\ -90° \le \phi \le 0°)$ and $(-90° \le \theta \le 0°,\ -90° \le \phi \le 0°)$.

10.1190/segam2019-3214439.1

Examples

In the previous section, we discuss only the propagator itself based on equation 1. The examples in this paper are implemented with some pre-processing and/or post-processing, e.g., phase rotation and angle and frequency filters. There are two examples. The first one is to show a comparison between the synthetic and theoretical snapshots. The theoretical result is calculated using the equation from Tsvankin (2005). The parameters that we use are v_p = 2000 m/s, ξ = 0.24, δ = 0.12, $\theta = -30°$, and $\varphi = 30°$. Figure 2 shows that our propagator using four-way splitting is accurate enough at depth 2000 m.

The second example involves a four-way FFD WEM image using 3D real data (Figure 3a). We use the TTI model for migration. We also present an RTM image (Figure 3b). Although we try to use the same parameters, some settings and processing of the RTM may be different from those of the WEM and so the RTM image is only used as a general reference. The four-way splitting FFD WEM can provide a good image. The red arrows denote the potential differences between the WEM and RTM images at the top salts. The stability of the WEM propagator is dependent on the FD order, grid interval, TTI parameters and so on. Occasionally, the WEM image may have big amplitudes due to the instability. This can be easily detected by outputting the maximum magnitude of the image for each shot. A solution is to use another group of parameters to redo the migration for that shot. For this example, there is only one shot, the image of which has a very small area in the deep part, with unreasonably high amplitudes; so, before stacking, for the image of that shot, we directly set the amplitudes below a certain depth to be zero. Note, although WEM is ideally free from the tomographic signals, a cheap and effective strategy (e.g., Zhang and Sun, 2009) to remove these signals is still useful. This is because the FFD formula approximates the decomposed full wave equation and so some tomographic signals may be left. For the WEM and RTM images, there are small differences in the implementation of the angle filter that is proposed by Zhang and Sun (2009), but the influence can be ignored.

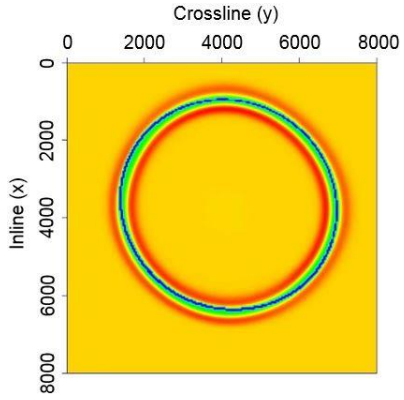

Figure 2: Comparison between the propagating wavefield (the rainbow curve) and the theoretical result (the blue curve) at depth 2000 m.

Conclusions

We develop an improved methodology for the coefficient estimation in the four-way splitting TTI FFD WEM. By selecting the phase angles, we give a linear approach to set up the initial values that are used as the input to the nonlinear inversion for the estimation of the coefficients. The entire coefficient-estimation flow consists of three steps: First, we select phase angles 0° and 90° to estimate the coefficients in the *x*- and *y*-directions; second, based on these coefficients, we select phase angles 45° and −45° to estimate the coefficients to compensate the propagation in the *m*- and *p*-directions. Certainly, the second step is a rough approximation; therefore, we use a third step, a nonlinear inversion, to improve the coefficient estimation. This scheme provides more accurate coefficients. We then describe a flow to implement the four-way splitting TTI FFD WEM. Some optimization strategies are also provided. Examples are presented to show the validity of the methodology and the flow.

Acknowledgments

The authors thank TGS and WesternGeco for the permission to publish this work. C. Tang also thanks C. Chiang, F. Hao, B. Wang, C. VanSchuyver and some other colleagues at TGS for the help.

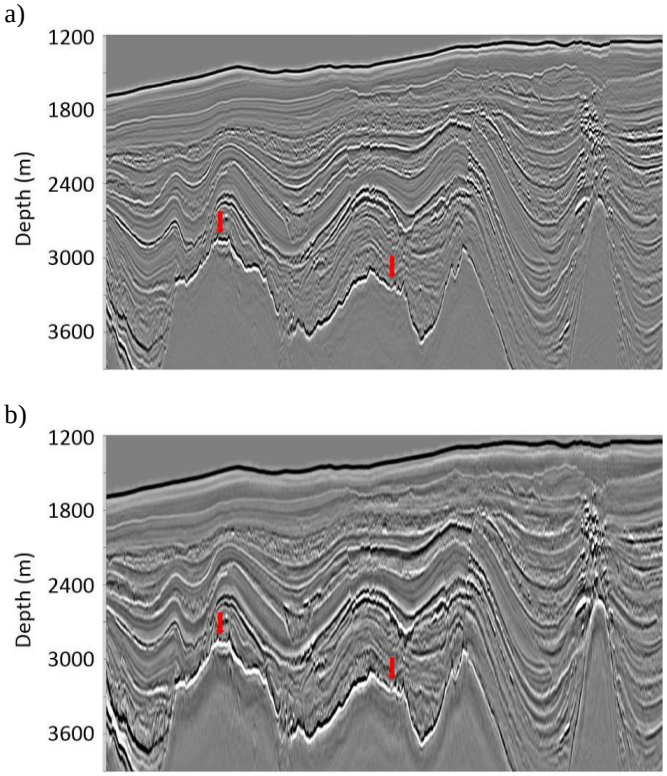

Figure 3: The image calculated by the four-way splitting FFD WEM (panel a) and the RTM (panel b) using the 3D FUSION data.

REFERENCES

Gazdag, J., 1978, Wave-equation migration by phase shift: Geophysics, **43**, 1342–1351, doi: https://doi.org/10.1190/1.1440899.

Hua, B., P., Williamson, B., Duquet, and J., Benamou, 2010, 3D TTI implicit finite difference migration with nonlinear optimized four-direction splitting expansion: 80th Annual International Meeting, SEG, Expanded Abstracts, 2082–2085, doi: https://doi.org/10.1190/1.3513530.

Hua, B., P., Williamson, B., Duquet, and H., Houllevigue, 2013, High-order and high-accuracy 3D Fourier finite difference depth migration with an optimally reduced coefficient table for tilted transversely isotropic media: 83rd Annual International Meeting, SEG, Expanded Abstracts, 3794–3798, doi: https://doi.org/10.1190/segam2013-1052.1.

Ristow, D., and T., Ruhl, 1994, Fourier finite-difference migration: Geophysics, **59**, 1882–1893, doi: https://doi.org/10.1190/1.1443575.

Ristow, D., and T., Ruhl, 1997, 3-D implicit finite-difference migration by multiway splitting: Geophysics, **62**, 554–567, doi: https://doi.org/10.1190/1.1444165.

Shan, G., 2006, Optimized implicit finite-difference migration for VTI media: 76th Annual International Meeting, SEG, Expanded Abstracts, 2367–2271, doi: https://doi.org/10.1190/1.2370010.

Shan, G., 2007, Optimized implicit finite-difference migration for TTI media: 77th Annual International Meeting, SEG, Expanded Abstracts, 2290–2293.

Tsvankin, I., 2005, Seismic signatures and analysis of reflection data in anisotropic media: Elsevier.

Valenciano, A. A., C. C., Cheng, N., Chemingui, and S., Brandsberg-Dahl, 2009, Fourier finite-difference migration for 3D TTI media: 71st Annual International Conference and Exhibition, EAGE, Expanded Abstracts, P065, doi: https://doi.org/10.3997/2214-4609.201400051.

Xie, X., and R., Wu, 1998, Improve the wide angle accuracy of screen method under large contrast: 68th Annual International Meeting, SEG, Expanded Abstracts, 1811–1814, doi: https://doi.org/10.1190/1.1820283.

Zhang, Y., and J., Sun, 2009, Practical issues of reverse time migration: True-amplitude gathers, noise removal and harmonic-source encoding: First Break, **27**, 53–59, doi: https://doi.org/10.3997/1365-2397.2009002.